nature COMMUNICATIONS

ARTICLE

https://doi.org/10.1038/s41467-021-23121-z OPEN

High-efficiency CO_2 separation using hybrid LDH-polymer membranes

Xiaozhi Xu[1], Jiajie Wang[1], Awu Zhou[2], Siyuan Dong[1], Kaiqiang Shi[1], Biao Li[1], Jingbin Han[1✉] & Dermot O'Hare[3✉]

Membrane-based gas separation exhibits many advantages over other conventional techniques; however, the construction of membranes with simultaneous high selectivity and permeability remains a major challenge. Herein, $(LDH/FAS)_n$-PDMS hybrid membranes, containing two-dimensional sub-nanometre channels were fabricated via self-assembly of unilamellar layered double hydroxide (LDH) nanosheets and formamidine sulfinic acid (FAS), followed by spray-coating with a poly(dimethylsiloxane) (PDMS) layer. A CO_2 transmission rate for $(LDH/FAS)_{25}$-PDMS of 7748 GPU together with CO_2 selectivity factors (SF) for SF (CO_2/H_2), SF(CO_2/N_2) and SF(CO_2/CH_4) mixtures as high as 43, 86 and 62 respectively are observed. The CO_2 permselectivity outperforms most reported systems and is higher than the Robeson or Freeman upper bound limits. These $(LDH/FAS)_n$-PDMS membranes are both thermally and mechanically robust maintaining their highly selective CO_2 separation performance during long-term operational testing. We believe this highly-efficient CO_2 separation performance is based on the synergy of enhanced solubility, diffusivity and chemical affinity for CO_2 in the sub-nanometre channels.

[1] State Key Laboratory of Chemical Resource Engineering, Beijing Advanced Innovation Center for Soft Matter Science and Engineering, Beijing University of Chemical Technology, Beijing, People's Republic of China. [2] Beijing Key Laboratory for Green Catalysis and Separation Department of Chemistry and Chemical Engineering, Beijing University of Technology, Beijing, People's Republic of China. [3] Chemistry Research Laboratory, Department of Chemistry University of Oxford, Oxford, UK. ✉email: hanjb@mail.buct.edu.cn; dermot.ohare@chem.ox.ac.uk

The separation of CO_2 is a crucial process for the purification of natural gas/syngas, flue gas recycling from thermal cracking and greenhouse gas mitigation[1–3]. Membrane-based CO_2 separation possesses a number of advantages, such as high-efficiency, simple process/equipment and low energy consumption[4,5]. Recently, two-dimensional (2D) nanosheet-based membranes have provoked wide attention for gas, liquid and ion separation[6–10]. Molecules located in these membranes transport through slit-like pores between stacked nanosheets or via micropores in the nanosheets. The size of the channels and physicochemical properties of the building blocks play key roles in determining permeability and selectivity of these membranes[11,12]. Porous 2D metal-organic framework (MOF) and zeolite-based membranes sieve gas molecules through their uniform micropores;[13,14] while non-porous graphene oxide (GO), MXene and layered transition-metal dichalcogenide nanosheets are normally fabricated as layered-stacking membranes to achieve gas separation[15–17]. Although excellent selectivity may be realised by such 2D membranes, they generally suffer from low permeability resulting from limited layered spacing and pore size[18–20]. Most of these 2D nanosheet-based membranes can only successfully achieve the separation of one or two of the three important binary gas mixtures; CO_2/H_2, CO_2/N_2 and CO_2/CH_4. In addition, the high cost and poor reproductivity of these membranes hinder their practical application. Therefore, there is still an urgent unmet need to develop high-performance membranes with simultaneously CO_2 high selectivity and permeability using cost-effective methods.

Exfoliated layered double hydroxide (LDH) nanosheets are regarded as ideal building blocks for ultrathin membranes[21,22]. Previously reported LDH membranes mainly used the interlayer CO_3^{2-} anion as the CO_2 carrier; it is not an efficient CO_2 transport carrier, and so leads to moderate CO_2 separation performance[10,23]. Reassembly of LDH host nanosheets with suitable guest molecules to construct superlattice membranes is an approach to precisely adjust the gallery height from nanometre to sub-nanometre scale[24]. In addition, a key feature of LDH nanosheets is their CO_2-philic nature due to their inherent basicity to bind acidic CO_2[25–28]. These physicochemical attributes allow us to facilitate CO_2 transport in LDH-based superlattice membranes. Another effective strategy to improve the permeability of CO_2 is the hybridisation with reactive carriers, such as amine and amidine functional groups into the membranes by virtue of their reversible reactivity towards CO_2[29,30]. However, the introduction of a large number of carrier pathways normally increases the disorder of the membranes, resulting in tortuous diffusion issues with resultant decreased transport rate for CO_2. One solution to this issue is the confinement of a CO_2 transport medium between lamellar-stacked LDH nanosheets to construct a highly oriented membrane with regular gas transport channels, to generate high-flux and highly selective gas permeability. However, such membranes have neither been proposed theoretically nor demonstrated experimentally.

Inspired by these concepts, we have fabricated 2D membranes with an ordered superlattice structure via alternating layer-by-layer (LBL) assembly of MgAl-LDH nanosheets and formamidine sulfinic acid (FAS), followed by coating a thin layer of poly (dimethylsiloxane) (PDMS) (Fig. 1 and Supplementary Fig. 1). Size-dependent gas diffusion was enhanced by tuning the parallel-stacked 2D channels with a suitable interlayer spacing. Chemical-selectivity was realised through the basic sites on the surface of CO_2-philic LDH laminates and CO_2 binding via amidine groups in the FAS layer. As a result, the synergistic effects among these functional elements induce an enhanced CO_2 separation performance, which surpasses the 2008 Robeson upper bound limits[31] and most of the previous reports.

Results and discussion

Microstructure and morphology of MgAl-LDH nanosheets. Monolayer LDH nanosheets were obtained by exfoliating a bulk sample in formamide. Highly crystalline, MgAl(CO_3)-LDH platelets were first prepared by a urea-assisted hydrothermal method[32]. X-ray diffraction (XRD) pattern of the MgAl(CO_3)-LDH (blue line in Fig. 2a) can be indexed as a prototypical layered structure exhibiting a harmonic series (00 l) of Bragg peaks at $2\theta = 12.1°$, 24.2°, 35.3°, 38.6°, 47.5° corresponding to the (003), (006), (012), (015), (018) Bragg reflections, respectively, in addition to Bragg peaks at $2\theta = 61.4°$ and 62.8° that index as the (110) and (113) reflections of the CO_3^{2-} intercalated hydrotalcite phase. The interlayer CO_3^{2-} was exchanged for NO_3^- by acid treatment under an N_2 atmosphere for ease of subsequent exfoliation. Compared with MgAl(CO_3)-LDH, the XRD pattern of MgAl(NO_3)-LDH (red line in Fig. 2a) shows a shift in the (003) Bragg reflection from $2\theta = 12.1°$ to 10.1°, indicating interlayer expansion and successful replacement of CO_3^{2-} by NO_3^-[33]. Top-view (along c-axis) scanning electron microscopy (SEM) image (Fig. 2b) reveals a hexagonal structure and primary platelet diameters in the range 1−3 μm, consistent with the average particle size of ~1.2 μm obtained by the dynamic light scattering (DLS) analysis (Supplementary Fig. 2). After delamination in formamide, the characteristic Bragg peaks associated with bulk LDH disappear (Supplementary Fig. 3), indicating a complete exfoliation of LDH platelets. The thick MgAl(NO_3)-LDH platelets were exfoliated into single-layer nanosheets with a thickness of ~0.8 nm, which gives an aspect ratio (platelet diameter/platelet thickness) of these nanosheets of *ca.* 450 (Fig. 2c). Additionally, high-resolution transmission electron microscopy (HRTEM) image (Supplementary Fig. 4) indicates the ultrathin nature and uniform thickness of the delaminated LDH nanosheets.

Preparation of the (LDH/FAS)$_n$-PDMS membranes. These ultra-high aspect ratio LDH nanosheets and FAS were alternatingly deposited to fabricate (LDH/FAS)$_n$ membranes by a LBL assembly method. The thickness of the membrane was controlled by changing the bilayer number n. After drying at room temperature (~25 °C) for 1 h, hydrated (LDH/FAS)$_n$ membranes were obtained due to the moisture-absorbing ability of the LDH nanosheets. A thin layer of PDMS was then deposited on the surface of (LDH/FAS)$_n$ to produce a locked-in heterostructure with consistent moisture content. The assembly process of the (LDH/FAS)$_n$ membranes was monitored by UV–Vis absorption spectroscopy. Figure 2d shows two absorption bands at 224 and 272 nm attributed to FAS[34], whose intensities increase almost linearly with the bilayer number (inset of Fig. 2d), indicating a successful step-by-step and controllable growth process. Fourier-transform infrared (FTIR) spectrum (Supplementary Fig. 5) of the as-prepared (LDH/FAS)$_n$ membrane exhibit strong absorption bands at 1640 and 3352 cm^{-1}, which are characteristic absorptions of C=N (thiol) and C−N (sulfhydryl) functional groups from FAS, respectively[35]. X-ray photoelectron spectroscopy (XPS) (Supplementary Figs. 6 and 7 and Table 1) indicates the formation of a strong electrostatic interaction between the anionic FAS and positively charged LDH nanosheets, we believe this strong interaction plays an important role in ensuring the stability of the membrane structure, which will be discussed later.

Top-view scanning electron microscopy (SEM) image (Fig. 3a) of the (LDH/FAS)$_{25}$ membrane reveals a densely covered surface without any visible defects or wrinkles. The optical image (Fig. 3a, inset) suggests good membrane homogeneity and flexibility. Side-view SEM image (Fig. 3b) shows a uniform membrane thickness of ~50 nm for (LDH/FAS)$_{60}$ with an interlocked lamellar structure. The cross-sectional HRTEM image (Fig. 3b, inset) reveals a high

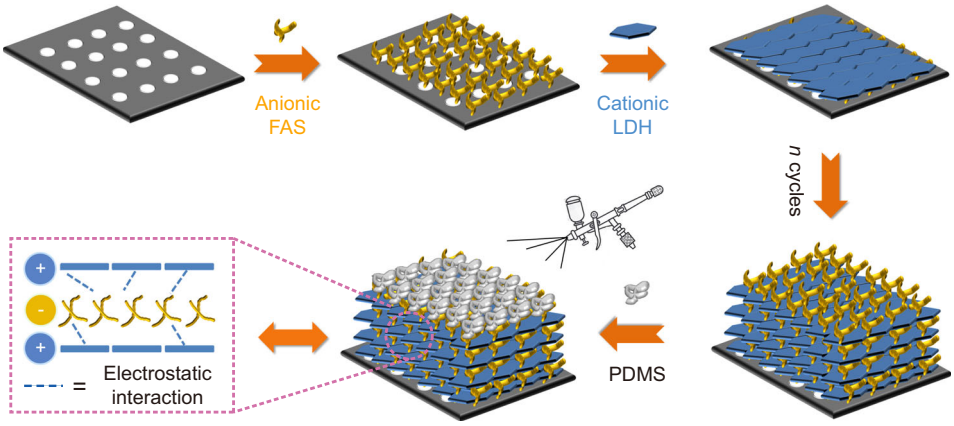

Fig. 1 Assembly of membranes. Schematic representation for the fabrication of $(LDH/FAS)_n$-PDMS membranes.

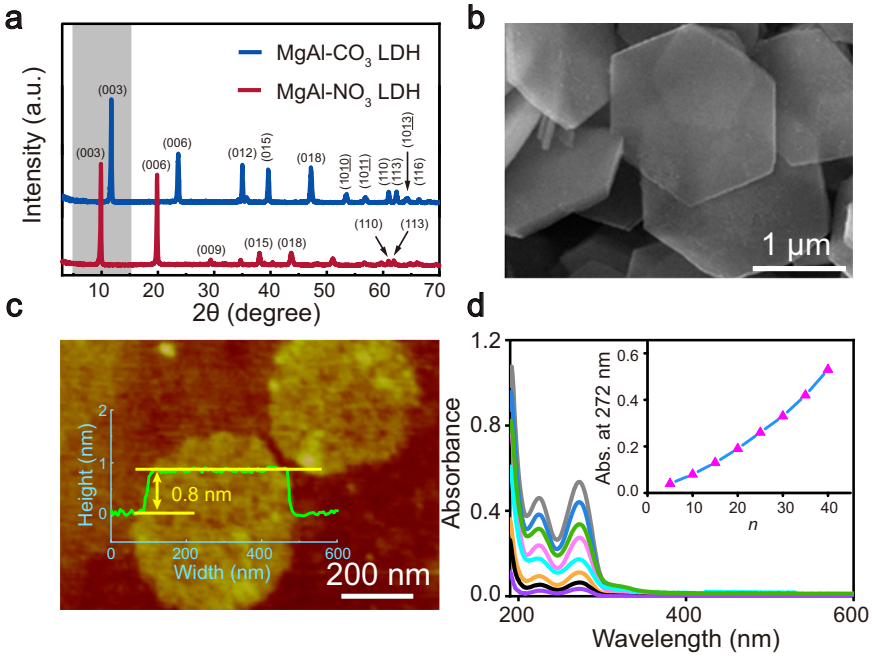

Fig. 2 Characterisation of LDH nanosheets and LBL assembly of $(LDH/FAS)_n$ membranes. a XRD patterns of $MgAl(CO_3)$-LDH and $MgAl(NO_3)$-LDH. **b** SEM images of $MgAl(NO_3)$-LDH. **c** Tapping-mode AFM image and height profiles of single-layer MgAl-LDH nanosheets. **d** UV–Vis absorption spectra of the $(LDH/FAS)_n$ membranes (inset: the approximately linear relationship between absorbance at 272 nm and bilayer number *n*).

nanosheet preferred orientation, highly ordered sub-nanometre channels as result of periodic stacking of LDH nanosheets and FAS.

The powder XRD of the membrane (Fig. 3c) contains a Bragg reflection at $2\theta = 10.76°$, which we attribute to a periodic repeat length of 0.82 nm from the assembled multilayer. The appearance of this broad Bragg diffraction feature demonstrates significant long-range order arising from parallel alignment of the LDH nanosheets on the substrate. The overall thickness of the structure may be obtained by multiplying the interlayer spacing and the number of bilayers, which is in good agreement with the result observed by cross-sectional SEM image. By subtracting the thickness of 0.48 nm for one single-layer LDH nanosheets[36], the distance between the adjacent LDH nanosheets is estimated to be 0.34 nm, as shown in Fig. 3d. In view of the kinetic diameter of CO_2 (0.33 nm), this gallery height is advantageous for the separation of CO_2 and other gases with kinetic diameters larger than this interlayer separation.

After coating with PDMS, the wettability of the hybrid membrane changed from hydrophilic to hydrophobic, the water contact angle increasing from 33.8° to 112.6° (Supplementary Fig. 8). Thermogravimetric analysis (TGA) (Supplementary Fig. 9) shows a large weight loss (~23%) at 100 °C for the $(LDH/FAS)_{25}$ membrane, indicating a highly hydrated state. Membranes with different numbers of assembly layers were also measured, these samples showed negligible % differences in weight loss from room temperature to 100 °C (Supplementary Fig. 10), indicating a similar presence of water content in $(LDH/FAS)_n$ membranes with different values of *n*. In contrast, the $(LDH/FAS)_{25}$-PDMS membrane only displayed ~2% weight reduction under the same conditions but does show a significant weight loss when heated above 120 °C. The inhibition of water desorption from the $(LDH/FAS)_{25}$-PDMS membrane is ascribed to a high water vapour barrier property of the hydrophobic PDMS coating. We found the retention of water within the $(LDH/FAS)_n$-PDMS membrane was an important attribute for the CO_2 separation performance, which will be discussed in the following sections.

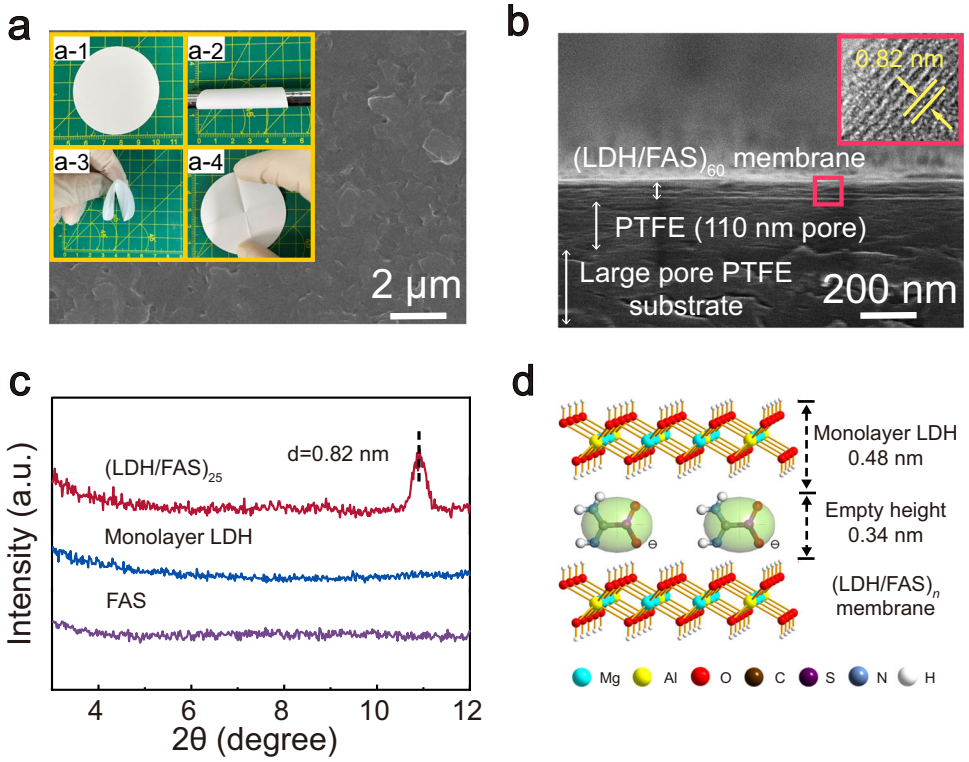

Fig. 3 Morphology and structure of (LDH/FAS)$_n$ membranes. a Top-view SEM image of (LDH/FAS)$_{25}$ membrane (The inset photographs show the membrane can be rolled onto a tube and returned to its original shape after bending.). **b** Cross-sectional SEM image of (LDH/FAS)$_{60}$ membrane (inset: HRTEM image). **c** XRD patterns for FAS, monolayer LDH nanosheets and (LDH/FAS)$_{25}$ membrane. **d** Schematic diagram of one bilayer of LDH/FAS.

Gas separation performance. The permeance of individual gases through the (LDH/FAS)$_n$-PDMS membranes with different bilayer numbers ($n = 5 - 25$) was investigated. The permeance of H_2, N_2 and CH_4 and CO_2 were measured, as these are the main components of natural gas, syngas, and flue gas from cracking. The gas transmission rate of an untreated poly(tetrafluoroethylene) (PTFE) substrate is 10^8 GPU (1 GPU = 1×10^{-6} cm^3 (STP) cm^{-2} s^{-1} cm Hg^{-1}), illustrating this substrate is almost fully permeable to these gas molecules. After deposition of the (LDH/FAS)$_n$-PDMS membranes, the transmission rates for H_2, N_2, CO_2 and CH_4 were all dramatically reduced with increasing n from 5 to 25 (Fig. 4a) due to the introduction of a physical barrier[37,38]. With $n = 5$, gas transmission rates were in the order $H_2 > CO_2 > N_2 > CH_4$. This indicates the gas transmission shows size-dependent selectivity when the membrane is thin, by considering the diameters of these gas molecules (H_2: 0.289 nm, CO_2: 0.33 nm, N_2: 0.364 nm, CH_4: 0.38 nm)[9]. The CO_2 transmission rate (CO_2TR) of the (LDH/FAS)$_{25}$-PDMS membranes decreases at a lower rate than those of other gases when the bilayer number exceeds 10, because of the selective permeance of CO_2 molecules. The (LDH/FAS)$_n$-PDMS membrane with $n = 25$ shows high selectivity for CO_2 transport, with a CO_2TR of 7748 GPU that is remarkably higher than H_2TR (180 GPU), N_2TR (91 GPU) and CH_4TR (124 GPU) (green line in Supplementary Fig. 11).

The CO_2 selectivity for the (LDH/FAS)$_n$-PDMS membranes was evaluated by computing a relative selectivity factor (SF) (Eq. 1):

$$\mathrm{SF}(\mathrm{CO_2}/\mathrm{other\ gas}) = \frac{\mathrm{CO_2TR}}{\mathrm{GTR}} \quad (1)$$

where CO_2TR is the CO_2 transmission rate, and GTR is the transmission rate of other gases (H_2, N_2 and CH_4). Upon increasing n from 5 to 25, the (LDH/FAS)$_n$-PDMS membrane exhibits an enhanced SF(CO_2/H_2), SF(CO_2/N_2) and SF(CO_2/CH_4) from 0.6, 0.9 and 0.8 to 43, 86 and 62, respectively (Fig. 4a). The separation performance of the (LDH/FAS)$_{25}$-PDMS membrane for CO_2/N_2 (Fig. 4b) and CO_2/CH_4 (Fig. 4c) is shown in the Robeson upper bound (2008) diagrams[31]. Owing to the lack of Robeson upper bound in the CO_2/H_2 system, a permeability/selectivity map reported by Freeman et al.[39] in 2006 was applied to evaluate the CO_2/H_2 separation performance of our membrane (Fig. 3d). Comparison of these upper bound lines and with other membrane materials in the literature[40–46], the CO_2 permselectivity of (LDH/FAS)$_{25}$-PDMS membrane outperforms most of the reported systems and is higher than the Robeson or Freeman upper bound limits. These results reveal that the (LDH/FAS)$_{25}$-PDMS membrane overcomes the "trade-off" between permeability and selectivity, as so provides the basis for an efficient CO_2 separation material for industrial gas mixtures. Upon further increasing the bilayer number greater than 25, a downward trend in the permeance was observed. A bilayer number of 25 seems to strike the optimum balance between permeability and selectivity.

When a 1:1:1:1 mixture of H_2, N_2, CH_4 and CO_2 (25% by partial pressure) was exposed to the (LDH/FAS)$_n$-PDMS membranes the permeance for all these gases was lower than that for individual pure gas (brown line in Supplementary Fig. 11), due to the competitive adsorption of different gases[47,48]. In spite of this, the (LDH/FAS)$_n$-PDMS membranes exhibited excellent CO_2 permselectivity for the four mixed gas systems. As shown in Fig. 5a, when the number of bilayers is low ($n = 5$), in the membrane transported gas was 33.1%, 22%, 25.2% and 19.7% for H_2, N_2, CH_4 and CO_2 respectively. With increasing membrane thickness, the penetration for all the gases decreases (Fig. 5b), similar to the results in pure gas. However, the permeance of H_2, CH_4 and N_2 decreases at much faster rates than

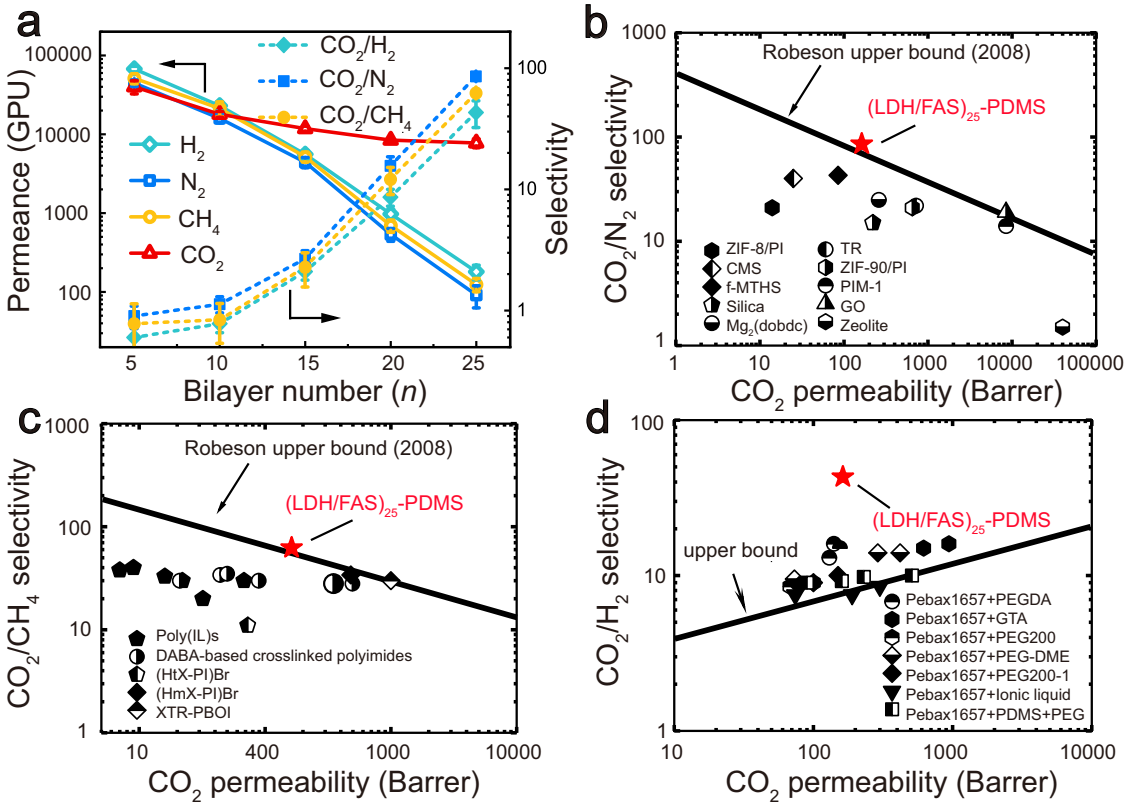

Fig. 4 Permeability and selectivity for pure gases. a The H_2, CO_2, N_2, CH_4 permeance and CO_2/H_2, CO_2/N_2, CO_2/CH_4 selectivity for $(LDH/FAS)_n$-PDMS membrane, 27 kPa; 298 K. **b** CO_2/N_2, **c** CO_2/CH_4 and **d** CO_2/H_2 separation performance of $(LDH/FAS)_{25}$-PDMS membrane and representative membranes reported in the literature.

for CO_2, so overall the CO_2 selectivity increases (Fig. 5c) and the proportion of CO_2 in the filtered gas is far larger when $n = 25$. Upon increasing the bilayer number from 5 to 25, the proportions of H_2, N_2 and CH_4 decrease stepwise to 2.3%, 1.2% and 1.6%, respectively. In contrast, the proportion of CO_2 in the membrane filtered gas increases rapidly from 19.7% to 94.9% to ultimately give outstanding CO_2 selectivity. The $(LDH/FAS)_n$-PDMS membranes also show acceptable CO_2 permeance (1938 GPU) when $n = 25$.

Gas separation mechanism. Solubility and diffusivity are two key parameters for gas separation performance[48,49]. An affinity of CO_2 for the membrane favours increased solubility selectivity. Preferential adsorption of the $(LDH/FAS)_{25}$-PDMS membrane was investigated using a mixture of CO_2/N_2. A typical adsorption isotherm is shown in Fig. 6a, which exhibits a much larger CO_2 adsorption than that of N_2. In addition, the CO_2 temperature programmed desorption (TPD) profile (Supplementary Fig. 12) of MgAl-LDH shows two maximum adsorption peaks at 158 °C and 176 °C, attributed to weak (hydroxyl groups on the LDH surface) and medium intensity (Mg^{2+}-O^{2-} pairs with high coordination) basic sites, respectively[50]. The affinity between CO_2 and membrane was further confirmed by Fourier-transform infrared (FT-IR) spectroscopy (Supplementary Fig. 13), which shows $\delta(CO_2)_{oop}$ adsorption band at 835 cm^{-1} (ascribed to the bicarbonate species[51]) when the membrane was exposed to CO_2 atmosphere. These results indicate that LDH has a certain CO_2 adsorption capacity and can reversibly interact with the acidic CO_2, so that the CO_2 molecules can preferentially accumulate on the LDH nanosheets and move freely and quickly within the hybrid membrane.

We believe that sub-nanometre channels within the membrane can serve as sieving pathways for these gases, allowing only molecules smaller than the height of the channels to permeate. The alternate stacking of the LDH nanosheets and FAS yields a layer spacing of 0.34 nm, this creates a permeation cut-off when the molecular dynamic diameter of the gas is bigger than this value (CH_4 and N_2 in this study). In addition, the interlocked layered structure containing nanosheets parallel to the substrate is beneficial to reduce the out-of-plane defects and inhibits the diffusion of larger gas molecules. To provide further support for a size-sieving function for these 2D nanochannels, a pure LDH nanosheet stacked membrane was prepared using a vacuum filtration method (Supplementary Fig. 14). This membrane displays selectivity (Supplementary Fig. 15) for H_2 permeation using mixtures of either H_2/N_2 or H_2/CH_4. The ability of these LDH membranes to allow the permeation of H_2 but rejection to N_2 and CH_4 is entirely consistent with the free distance of 0.30 nm for these LDH membranes. This value lies so between the dynamic diameter of H_2 and N_2 or CH_4. Furthermore, we performed CO_2 separation performance experiments on a disordered NO_3-LDH/FAS-PDMS membrane and found that such membrane showed CO_2 permeability but poor CO_2/N_2 selectivity (Supplementary Fig. 16), which further indicates that the regular nanochannels between LDH layers are essential to achieve high-efficiency CO_2 separation.

The solution/diffusion coefficients of CO_2 and N_2 in the hybrid LDH/FAS membranes were investigated via the time-lag method[52]. While the solubility coefficient and so penetration for CO_2 increases as the number of bilayers within the membrane increases (Supplementary Fig. 17) due to the accumulation of CO_2-philic LDH nanosheets. There is also a competing tortuosity/barrier effect[53], arising from horizontally oriented

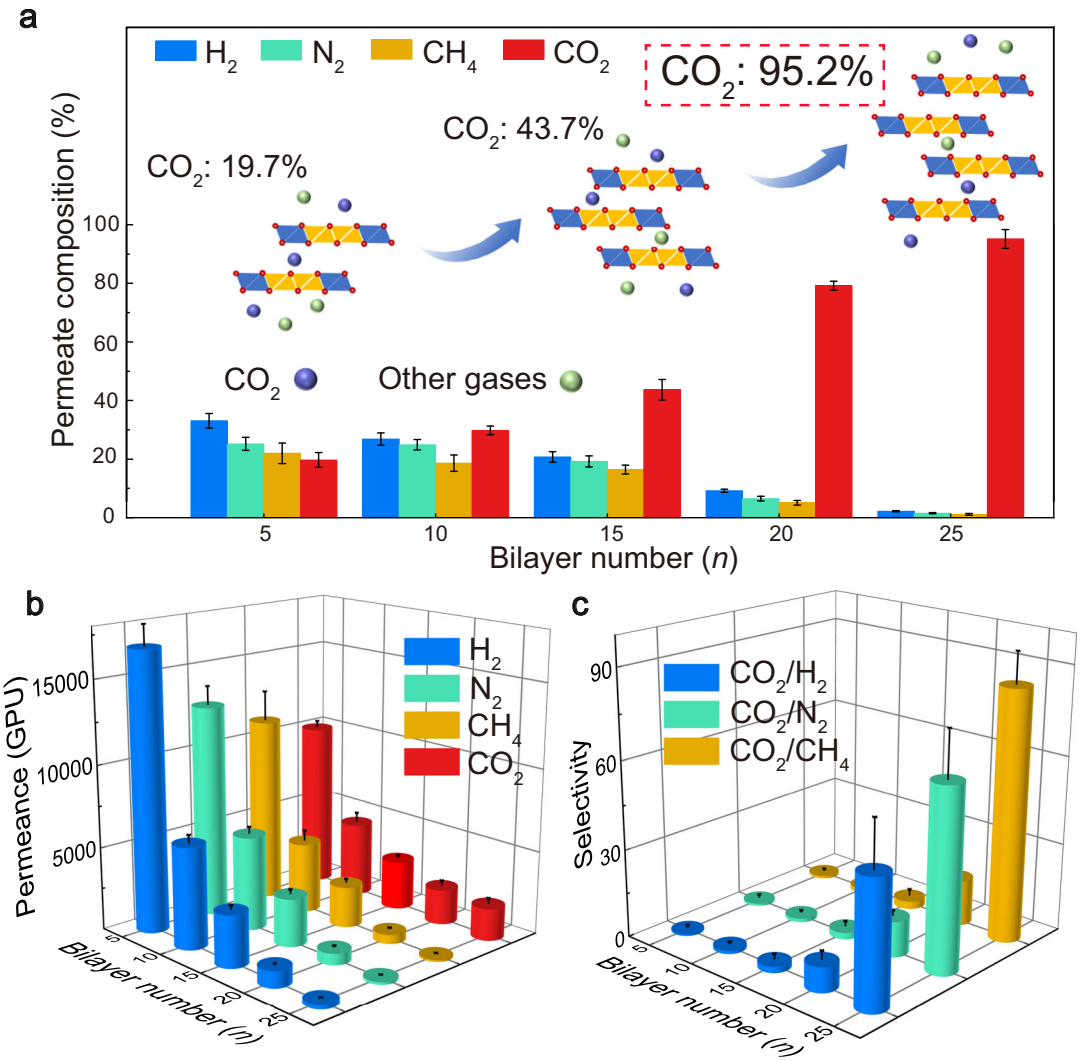

Fig. 5 Mixed gas separation performance of (LDH/FAS)$_n$-PDMS membranes. a The H_2, CO_2, N_2, CH_4 contents in the filtered gas for (LDH/FAS)$_n$-PDMS membranes under mixed gas feed conditions. **b** The H_2, CO_2, N_2, CH_4 transmission rates and **c** the CO_2/H_2, CO_2/N_2, CO_2/CH_4 selectivity for (LDH/FAS)$_n$-PDMS membranes. Feed gas: 25% CO_2, 25% N_2, 25% CH_4 and 25% H_2; 27 kPa; 298 K.

LDH nanosheet. Therefore, the diffusion coefficients for both CO_2 and N_2 decrease (Supplementary Fig. 18) with increasing n due to the creation of an increased physical barrier of LDH nanosheets. However, the CO_2/N_2 diffusion coefficient ratio increases, because the nanosheets do not restrict the diffusion of the smaller CO_2 as much.

As discussed earlier, the transmission rate for CO_2 is much higher than that of H_2 when the number of bilayers within the membrane exceeds 10, in spite of the smaller molecular size of H_2. This counterintuitive behaviour suggests other factors may be facilitating CO_2 transport. We believe FAS can act as an effective CO_2 carrier because of the reversible reaction between the amidine groups and CO_2 in aqueous solution[54–56], as shown in Equation 2 below:

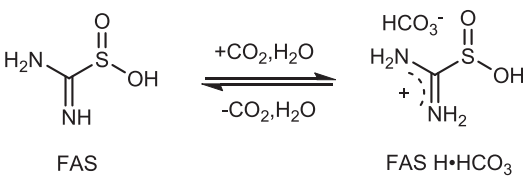

(2)

To probe the role of FAS for CO_2 transport, we studied the interaction between CO_2 and the thin membrane. In situ diffuse reflectance infrared Fourier-transform spectroscopy (DRIFTS) was used to monitor the membrane during CO_2 diffusion. Figure 6b shows the intensity of the absorption bands due to the protonated C=N group (1652 cm^{-1}) and bicarbonate (1599 cm^{-1})[35] increase when CO_2 is exposed to the membrane. In addition, the intensities of two broad absorption bands assigned to bidentate carbonate and bicarbonate at 1310 and 1190 cm^{-1} derived from the CO_2 adsorption onto the LDH[57,58], also increased. When He was introduced instead of CO_2, the intensities of these peaks gradually returned to the original intensities. These results indicate that the amidine groups within the membrane are reactive to CO_2 with high reversibility, and these groups actively contribute to the high-efficiency of the membrane for CO_2 separation. In addition, Supplementary Fig. 19 shows the CO_2 permeance of the (LDH/FAS)$_{25}$-PDMS membrane decreases with the increase of feed pressure and the decreasing trend slows down under high pressure, further confirming the permeation of CO_2 follows facilitated transport mechanism due to the reversible reaction as shown in Equation 2.

In order to further probe the apparent CO_2-facilitated transport through these (LDH/FAS)$_n$-PDMS membranes, we conducted temperature-dependent permeation at 27 kPa. The

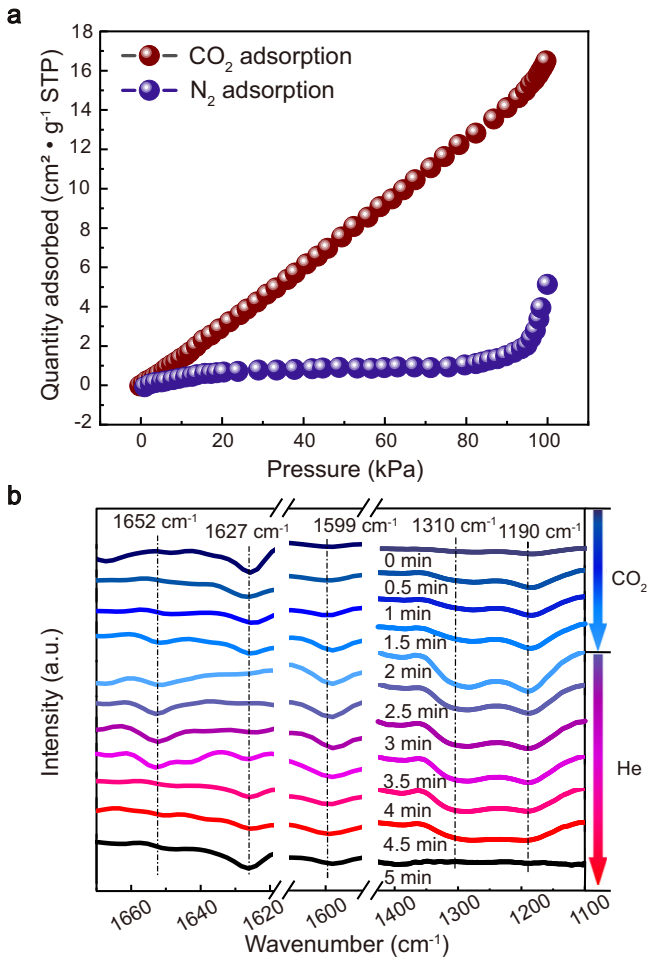

Fig. 6 Study on CO_2 selective transmission mechanism. a Pure-component CO_2 and N_2 adsorption in $(LDH/FAS)_{25}$-PDMS membrane. **b** In situ DRIFTS spectra of $(LDH/FAS)_{25}$-PDMS membrane upon CO_2 (within 0−2 min) adsorption and subsequent He adsorption (within 2−5 min).

effect of temperature on CO_2 permeability and CO_2/N_2 selectivity is shown in Supplementary Fig. 20, we also investigated the activation energy for CO_2 permeation. The permeability of CO_2 increases exponentially with increasing temperature and follows an Arrhenius relationship, indicating activated diffusion of CO_2 in the membrane. The activation energy for CO_2 diffusion in the $(LDH/FAS)_n$-PDMS membrane is at least 8.0 kJ mol^{-1} higher than that of N_2 (see Supplementary Information), which results in the trend of increasing selectivity of CO_2/N_2 with increasing temperature. These results indicate an increase in CO_2 permeability caused by the facilitated transport is much faster than the increase in N_2 permeability induced by thermally activated diffusion rates.

Following the construction of alternating $(LDH/FAS)_n$ layers using the LBL process, the subsequent coating of this hybrid layer structure with PDMS plays an important role in the selective transport of CO_2. As discussed above, the reversible reaction between CO_2 and FAS requires water, and so the PDMS coating plays a key role as a moisture vapour-blocking layer, inhibiting diffusional loss of water within the membranes. Without PDMS coating, the $(LDH/FAS)_n$ membranes would rapidly dehydrate when heated at ~50 °C for 30 min (the same drying condition to obtain PDMS coated membranes).

To investigate the influence of water content on the separation performance of the $(LDH/FAS)_n$ membranes, a series of $(LDH/FAS)_n$ membranes with different degrees of hydration were prepared by controlling the drying temperature (Supplementary Table 2). Upon decreasing the membrane water content (25–0%), the CO_2 permeance drops dramatically from 7748 to 217 GPU. These results confirm that the presence of water is a key component in facilitating transport in these membranes.

The gas transport behaviour of a fully dehydrated $(LDH/FAS)_{25}$ membrane for H_2, N_2, CH_4 was also investigated. We find that this membrane still shows a molecular sieving effect (Supplementary Fig. 21). The temperature dependence (25–80 °C) of the selectivity of CO_2 vs. N_2 for the fully dehydrated $(LDH/FAS)_{25}$ membrane did not change whereas the permeability of CO_2 and N_2 doubled (Supplementary Fig. 22). In the absence of water, gas permeability is thought to be just thermally activated.

Although $(LDH/FAS)_n$-PDMS membranes are thermally robust, heating to 150 °C for 30 min results in decreased membrane performance (Supplementary Fig. 23). $(LDH/FAS)_n$-PDMS membranes can retain the necessary degree of hydration within the membrane structure and so can effectively operate with a dry gas feed. Typically, the presence of water vapour in feed gas condenses on membrane surfaces or pores, which deteriorates the permeability or selectivity of membrane materials. Pure PDMS membranes exhibit high gas permeance but low permselectivity for CO_2 (Supplementary Fig. 24), which further supports the suggestion that the primary function of PDMS is preventing water evaporation from the hydrated membrane without unduly affecting the gas permeation.

The selective transmission of CO_2 is ascribed to be based on the synergy of solubility selectivity, diffusivity selectivity and reaction selectivity. For larger molecules, such as CH_4 and N_2, their transmission is selectively blocked by the sub-nanometre channels and the barrier effect imposed by the LDH nanosheets. As a result, their transmission follows the classic solution-diffusion mechanism. For H_2 with a smaller size than the height of channels, it is not adequately blocked by the sub-nanometre channels and LDH nanosheets, and some H_2 penetrates the membrane. Facilitated transport, as introduced by FAS provides reaction selectivity of CO_2. Taking into consideration these different factors, high-efficiency CO_2 separation is achieved using $(LDH/FAS)_{25}$-PDMS membrane.

In order to investigate the potential practical applications of $(LDH/FAS)_{25}$-PDMS membranes, a series of operational stability tests were conducted. Supplementary Fig. 25 illustrates that the $(LDH/FAS)_{25}$-PDMS membrane maintains the high separation performance of CO_2/H_2, CO_2/N_2 and CO_2/CH_4 during a 120 h operational test. Meanwhile, the membrane does not exhibit obvious surface damage (Supplementary Fig. 26) after continuous gas permeation for 120 h, indicating good chemical compatibility and high mechanical stability. Even treated under a higher temperature of 80 °C, the $(LDH/FAS)_n$-PDMS membrane is still intact without defects and the building units are well-bonded with each other without falling off, demonstrating good thermal stability (Supplementary Fig. 27). The remarkable stability may be attributed to the creation of strong electrostatic anion-layer interactions by partial deprotonation of the FAS. However, to achieve industrial application, the energy consumption and environmental impacts for the separation process should be evaluated using life cycle assessment and energetic analysis method. The regeneration of fouled membranes should also be considered, such as by thermal regeneration or chemical regeneration techniques. To provide further support to the sugnificant role of the electrostatic interaction between the building units in these 2D heterostructures, new membranes were prepared by using graphene oxide (GO) instead of the LDH

nanosheets via the same fabrication method to give $(GO/FAS)_n$-PDMS.

The XRD of the $(GO/FAS)_n$-PDMS membranes displayed a Bragg reflection corresponding to a *d*-spacing of 0.76 nm (Supplementary Fig. 28). By subtracting the thickness of a GO layer (0.35 nm) we can estimate the interlayer channel thickness. The channel thickness in $(GO/FAS)_n$-PDMS is larger (0.41 nm) than that of $(LDH/FAS)_n$-PDMS (0.34 nm). We attribute this to the absence of any significant electrostatic interactions between GO and FAS (Supplementary Fig. 29 and Table 3). We also find that $(GO/FAS)_n$-PDMS membranes exhibit poor stability during long-term gas permeation tests (Supplementary Fig. 30). Furthermore, very small differences between the permeation of H_2, CO_2, N_2 and CH_4 through $(GO/FAS)_n$-PDMS membranes are observed.

In conclusion, we show that single-layer LDH nanosheets and FAS superlattice structures fabricated by LBL assembly can be effective CO_2 separation membranes. The membrane performance was optimised by controlling the balance between gas barrier and transmission. The PDMS coated membrane, $(LDH/FAS)_{25}$-PDMS exhibits excellent CO_2 preferential permeability with ultra-high CO_2/N_2, CO_2/H_2 and CO_2/CH_4 selectivity, exceeding the Robeson 2008 upper bond. The sub-nanometre channels between LDH and FAS act to produce a size-selective architecture for gas sieving; while the hydroxyl groups in the LDH nanosheets increase the affinity of CO_2 sorption, leading to improved solubility. We believe the amidine groups present in the FAS located between the LDH nanosheets can reversibly bind CO_2 selectively thus promoting the selective transport of CO_2 over either N_2, CH_4 or H_2. Furthermore, the $(LDH/FAS)_n$-PDMS membranes are mechanically robust and maintain their high separation performance during long-term operational testing. By considering the building units are all cheap industrial raw materials, and the membranes are easy to prepare on various substrates, it is possible to realise large-scale membranes manufacturing. We believe these hybrid lamellar membrane heterostructures hold great potential for CO_2 capture and separation.

Methods

Reagents and materials. Formamidine sulfinic acid (FAS) and poly(dimethylsiloxane) (PDMS) with a molecular weight of ~50,000 were purchased from Aladdin (Beijing, China). PTFE substrates (thickness: ~200 μm; average pore size: ~220 nm) were obtained from Sigma-Aldrich company. Single-layered graphene oxide (GO) nanosheets was provided by XFNANO (Nanjing, China). Pure N_2, CH_4, H_2 and CO_2 gases with purity of 99.999% and $CO_2/N_2/H_2/CH_4$ mixed gases (25/25/25/25 by volume) were purchased from Beijing ZG Special Gases Science & Technology Co. Ltd. The following analytical grade chemicals were used without further purification: urea, $NaNO_3$, $Mg(NO_3)_2{\cdot}6H_2O$, HNO_3, H_2SO_4, $Al(NO_3)_3{\cdot}9H_2O$, ethanol and acetone. Deionized water was used in all the experiments.

Synthesis of MgAl-LDH nanoplatelets. $MgAl(CO_3)$-LDH nanoplatelets were synthesised by an urea-assisted hydrothermal method[32]. Typically, $Al(NO_3)_3{\cdot}9H_2O$, $Mg(NO_3)_2{\cdot}6H_2O$ and urea were dissolved in 100 mL deionized water with concentrations of 0.05, 0.1 and 0.5 M, respectively. The mixed solution was transferred into a stainless steel autoclave with a Teflon lining and then hydrothermally treated at 110 °C for 24 h. The obtained $MgAl(CO_3)$-LDH was washed with water and anhydrous ethanol three times, and then dried at room temperature for 48 h. For ease of exfoliation, the $MgAl(CO_3)$-LDH was anion exchanged into $MgAl(NO_3)$-LDH by a salt-acid method reported previously[36]. Typically, 1.0 g $MgAl(CO_3)$-LDH and 1 L salt-acid solution ($NaNO_3$: 1.5 mol and HNO_3: 0.0045 mol) were mixed and stirred under the N_2 gas flow for 24 h. The resulting $MgAl(NO_3)$-LDH nanoplatelets were centrifuged, washed and vacuum-dried.

Exfoliation of LDH nanoplatelets into monolayer nanosheets. In all, 0.1 g $MgAl(NO_3)$-LDH was strongly agitated in 100 mL formamide for 48 h. A colloidal suspension of positively charged and unilaminar MgAl-LDH nanosheets was successfully prepared with a concentration of 1 g L^{-1}.

Fabrication of the $(LDH/FAS)_n$-PDMS membrane. The layer-by-layer (LBL) deposition and spray-coating techniques were adopted to fabricate the $(LDH/FAS)_n$-PDMS membranes. Quartz glass and silicon wafer were used as substrates for UV–Vis spectra, SEM and AFM characterisation, respectively. The PTFE substrate was chosen for the other measurements. Prior to deposition, quartz glass and silicon wafer were washed in ethanol, acetone and deionized water for 15 min, respectively. The PTFE substrate was washed using deionized water for 5 min. The LBL assembly process was as follows: the substrate was dipped in the resulting $MgAl(NO_3)$-LDH colloidal suspension (1 mg mL^{-1}) for 10 min followed by washing thoroughly, and then the substrate was immersed into FAS aqueous solution (2.0 g L^{-1}) for 10 min. The $(LDH/FAS)_n$ membranes were fabricated by alternate deposition of LDH nanosheets and FAS for *n* cycles. The as-prepared $(LDH/FAS)_n$ membranes were dried at room temperature (~25 °C) for 1 h unless otherwise stated. Ultimately, a thin layer of PDMS was deposited on the $(LDH/FAS)_n$ membrane surface using an airbrush style spray-gun (3 applications) and a spin-coater (1000 rpm, 1 min). The obtained $(LDH/FAS)_n$-PDMS membranes were dried at 50 °C for 30 min.

Fabrication of the disordered NO_3-LDH/FAS-PDMS membrane. FAS aqueous solution (2.0 g L^{-1}) was added into $MgAl(NO_3)$-LDH suspension (1.0 g L^{-1}) with a volume ratio of 1:1, followed by stirring at room temperature for 12 h. Then the NO_3-LDH/FAS dispersion was cast on PTFE substrate to prepare composite membranes. The NO_3-LDH/FAS membrane was dried at room temperature (~25 °C) for 1 h. Ultimately, a thin layer of PDMS was deposited on the NO_3-LDH/FAS membrane via spray and spin coating steps.

Fabrication of pure LDH membrane. The LDH membrane was prepared by depositing a colloidal suspension of $MgAl(NO_3)$-LDH (1 g L^{-1}) on PTFE substrates using vacuum-assisted suction filtration. The as-prepared LDH membranes were dried at room temperature (~25 °C) for 1 h.

Fabrication of $(GO/FAS)_n$-PDMS membrane. A similar method combining LBL deposition and spray-coating was applied to prepare $(GO/FAS)_n$-PDMS membranes for comparison study, using GO colloidal suspension (1 g L^{-1}), FAS aqueous solution (2 g L^{-1}) and PDMS solution.

Characterisation techniques. XRD patterns were recorded by a Rigaku XRD-6000 diffractometer, using Cu Kα radiation ($\lambda = 0.1542$ nm) at 40 kV, 30 mA. The UV–Vis absorption spectra were collected in the range 200 − 800 nm on a Shimadzu U-3000 spectrophotometer. The morphology was investigated using a scanning electron microscope (SEM; Zeiss SUPRA 55) with an accelerating voltage of 20 kV, a FEI Cs-corrected Titan 80-300 high-resolution transmission electron microscope (HRTEM) operated at 300 kV and a NanoScope IIIa atomic force microscope (AFM) from Veeco Instruments. The FT-IR spectra were performed using a Vector 22 (Bruker) spectrophotometer with 2 cm^{-1} resolution. In situ DRIFTS of CO_2 and N_2 were performed on a VERTEX 70 (Bruker Company) spectrometer equipped with MCT narrowband detector and an in situ reaction cell. The preprocessing and testing details are as follows. Firstly, the membrane was carefully placed onto the support sheet of the reaction cell. Secondly, the sample was pre-processed in a He flow (50 mL min^{-1}) at 80 °C with a heating rate of 5 °C min^{-1}, followed by He purification (50 mL min^{-1}) for 1 h and cool to 25 °C. Subsequently, CO_2 was introduced into the cell, and then DRIFTS was collected every 30 s until the CO_2 adsorption signal remained unchanged. Finally, the gas flow was switched to high-purity He to collect desorption spectra every 30 s. Thermogravimetric analysis (TGA) was performed with a HCT-1 differential thermal gravimetric analyser (Beijing Henven Scientific Instrument Factory, Beijing, China). The particle size distribution of LDH nanoplates was measured with a Malvern Mastersizer 2000 analyser (Malvern Instruments Ltd., Malvern, UK). The gas (H_2, N_2, CO_2, and CH_4) transmission rates were measured using a VAC-V2 gas transmission rate testing system (Labthink Instruments Co., Ltd., Jinan, China). Solution/diffusion coefficients were obtained by Basic 201 gas transmission rate testing system (Labthink Instruments Co., Ltd., Jinan, China) via the time-lag method[52]. $DC = l^2/6\theta$, $SC = P/DC$, where DC is the diffusion coefficients, SC is the solution coefficients, P is the permeability, l is the film thickness, and θ is called time-lag. The gas transmission rates were tested at 23 °C and 0% relative humidity unless otherwise indicated. The content of each component for the mixed gas (CO_2, H_2, CH_4 and N_2) was obtained using a SCION 456-GC (Bruker) gas chromatography. The water contact angle (WCA) test was conducted using a DSA100 drop shape analysis system (KRüSS GmbH Company, Hamburg, Germany). The specific gas adsorption behaviour of the membrane was performed by adsorption experiment at 25 °C (ASAP 2020, Micromeritics, USA) using pure CO_2 and N_2. X-ray photoelectron spectra (XPS) measurements were performed (Thermo VG Escalab 250) at a pressure of about 2×10^{-9} Pa with Al Kα X-rays as the excitation source. Programmed Temperature Desorption (TPD) experiments were investigated using a Micromeritics Auto Chem II 2920 device with a thermal conductivity detector (TCD).

Data availability

The authors declare that the main data supporting the findings of this study are available within the article and its Supplementary Information files.

Received: 7 February 2021; Accepted: 15 April 2021;
Published online: 24 May 2021

References

1. Li, S. G., Falconer, J. L. & Noble, R. D. Improved SAPO-34 membranes for CO2/CH4 separations. *Adv. Mater.* **18**, 2601–2603 (2006).
2. Carreon, M. A., Li, S. G., Falconer, J. L. & Noble, R. D. SAPO-34 seeds and membranes prepared using multiple structure directing agents. *Adv. Mater.* **20**, 729–732 (2008).
3. Hao, G. P., Li, W. C., Qian, D. & Lu, A. H. Rapid synthesis of nitrogen-doped porous carbon monolith for CO2 capture. *Adv. Mater.* **22**, 853–857 (2010).
4. Park, H. B., Kamcev, J., Robeson, L. M., Elimelech, M. & Freeman, B. D. Maximizing the right stuff: the trade-off between membrane permeability and selectivity. *Science* **356**, 1137–1146 (2017).
5. Zhu, X. et al. A superacid-catalyzed synthesis of porous membranes based on triazine frameworks for CO2 separation. *J. Am. Chem. Soc.* **134**, 10478–10484 (2012).
6. Wang, S. et al. Graphene oxide membranes with heterogeneous nanodomains for efficient CO2 separations. *Angew. Chem. Int. Ed.* **56**, 14246–14251 (2017).
7. Chen, L. et al. Ion sieving in graphene oxide membranes via cationic control of interlayer spacing. *Nature* **550**, 380–383 (2017).
8. Nair, R. R., Wu, H. A., Jayaram, P. N., Grigorieva, I. V. & Geim, A. K. Unimpeded permeation of water through helium-leak-tight graphene-based membranes. *Science* **335**, 442–444 (2012).
9. Shen, J. et al. Subnanometer two-dimensional graphene oxide channels for ultrafast gas sieving. *ACS Nano* **10**, 3398–3409 (2016).
10. Liao, J. Y. et al. Fabrication of high-performance facilitated transport membranes for CO2 separation. *Chem. Sci.* **5**, 2843–2849 (2014).
11. Abraham, J. et al. Tunable sieving of ions using graphene oxide membranes. *Nat. Nanotech.* **12**, 546–550 (2017).
12. Meng, Y. et al. A high-flux mixed matrix nanofiltration membrane with highly water-dispersible MOF crystallites as filler. *J. Membr. Sci.* **591**, 117360–117368 (2019).
13. Peng, Y. et al. Metal-organic framework nanosheets as building blocks for molecular sieving membranes. *Science* **346**, 1356–1359 (2014).
14. Gascon, J. et al. Practical approach to zeolitic membranes and coatings: state of the art, opportunities, barriers, and future perspectives. *Chem. Mater.* **24**, 2829–2844 (2012).
15. Gascon, J. et al. MXene molecular sieving membranes for highly efficient gas separation. *Nat. Commun.* **9**, 155–162 (2018).
16. Wang, D., Wang, Z. G., Wang, L., Hu, L. & Jin, J. Ultrathin membranes of single-layered MoS2 nanosheets for high-permeance hydrogen separation. *Nanoscale* **7**, 17649–17652 (2015).
17. Li, H. et al. Ultrathin, molecular-sieving graphene oxide membranes for selective hydrogen separation. *Science* **342**, 95–98 (2013).
18. Perreault, F., de Faria, A. F. & Elimelech, M. Environmental applications of graphene-based nanomaterials. *Chem. Soc. Rev.* **44**, 5861–5896 (2015).
19. Zheng, Z., Grunker, R. & Feng, X. Synthetic two-dimensional materials: a new paradigm of membranes for ultimate separation. *Adv. Mater.* **28**, 6529–6545 (2016).
20. Liu, G., Jin, W. & Xu, N. Two-dimensional-material membranes: a new family of high-performance separation membranes. *Angew. Chem. Int. Ed.* **55**, 13384–13397 (2016).
21. Wang, J. et al. Zwitterionic functionalized layered double hydroxides nanosheets for a novel charged mosaic membrane with high salt permeability. *J. Membr. Sci.* **510**, 27–37 (2016).
22. Ang, E. H., Velioğlu, S. & Chew, J. W. Tunable affinity separation enables ultrafast solvent permeation through layered double hydroxide membranes. *J. Membr. Sci.* **591**, 117318–117327 (2019).
23. Liao, J. et al. A high performance PVAm-HT membrane containing high-speed facilitated transport channels for CO2 separation. *J. Mater. Chem. A* **3**, 16746–16761 (2015).
24. Yan, D. et al. Ordered poly(p-phenylene)/layered double hydroxide ultrathin films with blue luminescence by layer-by-layer assembly. *Angew. Chem. Int. Ed.* **48**, 3073–3076 (2009).
25. Liu, Y. et al. 2D layered double hydroxide membranes with intrinsic breathing effect toward CO2 for efficient carbon capture. *J. Membr. Sci.* **598**, 117663–117671 (2020).
26. Lu, P., Liu, Y., Zhou, T., Wang, Q. & Li, Y. Recent advances in layered double hydroxides (LDHs) as two-dimensional membrane materials for gas and liquid separations. *J. Membr. Sci.* **567**, 89–103 (2018).
27. Kim, T. W., Sahimi, M., Tsotsis & T., T. The preparation and characterization of hydrotalcite micromembranes. *Chem. Eur. J.* **64**, 1585–1590 (2009).
28. Dou, Y. et al. Transparent, ultrahigh-gas-barrier films with a brick-mortar-sand structure. *Angew. Chem. Int. Ed.* **54**, 9673–9678 (2015).
29. Qiao, Z. et al. PVAm-PIP/PS composite membrane with high performance for CO2/N2 separation. *AIChE J.* **59**, 215–228 (2013).
30. Wang, M. M. et al. A high performance antioxidative and acid resistant membrane prepared by interfacial polymerization for CO2 separation from flue gas. *Energy Environ. Sci.* **6**, 539–551 (2013).
31. Robeson, L. M. The upper bound revisited. *J. Membr. Sci.* **320**, 390–400 (2008).
32. Wang, J. et al. Moisture-permeable, humidity-enhanced gas barrier films based on organic/inorganic multilayers. *ACS Appl. Mater. Interfaces* **10**, 28130–28138 (2018).
33. Wang, Q. & O'Hare, D. Recent advances in the synthesis and application of layered double hydroxide (LDH) nanosheets. *Chem. Rev.* **112**, 4124–4155 (2012).
34. Darwish, T. A., Evans, R. A., James, M. & Hanley, T. L. Spiropyran-amidine: a molecular canary for visual detection of carbon dioxide gas. *Chem. Eur. J.* **17**, 11399–11404 (2011).
35. Furusho, Y. & Endo, T. Capture and release of CO2 by polyamidine. *J. Polym. Sci., Part A: Polym. Chem.* **51**, 3404–3411 (2013).
36. Liu, Z. et al. Synthesis, anion exchange, and delamination of Co-Al layered double hydroxide: assembly of the exfoliated nanosheet/polyanion composite films and magneto-optical studies. *J. Am. Chem. Soc.* **128**, 4872–4880 (2006).
37. Yang, Y. H., Bolling, L., Priolo, M. A. & Grunlan, J. C. Super gas barrier and selectivity of graphene oxide-polymer multilayer thin films. *Adv. Mater.* **25**, 503–508 (2013).
38. Kim, D. et al. Highly size-selective ionically crosslinked multilayer polymer films for light gas separation. *Adv. Mater.* **26**, 746–751 (2014).
39. Lin, H. Q., Van Wagner, E., Freeman, B. D., Toy, L. G. & Gupta, R. P. Plasticization-enhanced hydrogen purification using polymeric membranes. *Science* **311**, 639–642 (2006).
40. Budd, P. M. et al. Gas separation membranes from polymers of intrinsic microporosity. *J. Membr. Sci.* **251**, 263–269 (2005).
41. Park, H. B., Han, S. H., Jung, C. H., Lee, Y. M. & Hill, A. J. Thermally rearranged (TR) polymer membranes for CO2 separation. *J. Membr. Sci.* **359**, 11–24 (2010).
42. Hanioka, S. et al. CO2 separation facilitated by task-specific ionic liquids using a supported liquid membrane. *J. Membr. Sci.* **314**, 1–4 (2008).
43. Nugent, P. et al. Porous materials with optimal adsorption thermodynamics and kinetics for CO2 separation. *Nature* **495**, 80–84 (2013).
44. Qiao, Z. et al. Highly permeable aligned montmorillonite mixed-matrix membrane for CO2 separation. *Angew. Chem. Int. Ed.* **55**, 9321–9325 (2016).
45. Kammakakam, I., Yoon, H. W., Nam, S., Park, H. B. & Kim, T. H. Novel piperazinium-mediated crosslinked polyimide membranes for high performance CO2 separation. *J. Membr. Sci.* **487**, 90–98 (2015).
46. Shen, J. et al. Membranes with fast and selective gas-transport channels of laminar graphene oxide for efficient CO2 capture. *Angew. Chem. Int. Ed.* **54**, 578–582 (2015).
47. Li, W. et al. Ultrathin metal-organic framework membrane production by gel-vapour deposition. *Nat. Commun.* **8**, 406–414 (2017).
48. Li, X. et al. Efficient CO2 capture by functionalized graphene oxide nanosheets as fillers to fabricate multi-permselective mixed matrix membranes. *ACS Appl. Mater. Interfaces* **7**, 5528–5537 (2015).
49. Li, S., Wang, Z., Yu, X., Wang, J. & Wang, S. High-performance membranes with multi-permselectivity for CO2 separation. *Adv. Mater.* **24**, 3196–3200 (2012).
50. Sun, Z. et al. A structured catalyst based on cobalt phthalocyanine/calcined Mg-Al hydrotalcite film for the oxidation of mercaptan. *Green. Chem.* **14**, 1909–1916 (2012).
51. Baltrusaitis, J., Jensen, J. H. & Grassian, V. H. FTIR spectroscopy combined with isotope labeling and quantum chemical calculations to investigate adsorbed bicarbonate formation following reaction of carbon dioxide with surface hydroxyl groups on Fe2O3 and Al2O3. *J. Phys. Chem. B* **110**, 12005–12016 (2006).
52. Car, A., Stropnik, C., Yave, W. & Peinemann, K. V. PEG modified poly (amide-b-ethylene oxide) membranes for CO2 separation. *J. Membr. Sci.* **307**, 88–95 (2008).
53. Priolo, M. A., Holder, K. M., Guin, T. & Grunlan, J. C. Recent advances in gas barrier thin films via layer-by-layer assembly of polymers and platelets. *Macromol. Rapid. Commun.* **36**, 866–879 (2015).
54. Jessop, P. G., Heldebrant, D. J., Li, X., Eckert, C. A. & Liotta, C. L. Reversible nonpolar-to-polar solvent. *Nature* **436**, 1102–1102 (2005).
55. Liu, Y., Jessop, P. G., Cunningham, M., Eckert, C. A. & Liotta, C. L. Switchable surfactants. *Science* **313**, 958–960 (2006).
56. Quek, J. Y., Davis, T. P. & Lowe, A. B. Amidine functionality as a stimulus-responsive building block. *Chem. Soc. Rev.* **42**, 7326–7334 (2013).
57. Morikawa, M., Ahmed, N., Yoshida, Y. & Izumi, Y. Photoconversion of carbon dioxide in zinc-copper-gallium layered double hydroxides: The kinetics to hydrogen carbonate and further to CO/methanol. *Appl. Catal. B* **144**, 561–569 (2014).

58. León, M. et al. Adsorption of CO2 on hydrotalcite-derived mixed oxides: Sorption mechanisms and consequences for adsorption irreversibility. *Ind. Eng. Chem. Res.* **49**, 3663–3671 (2010).

Acknowledgements
This work was supported by the National Natural Science Foundation of China (21671015, 21521005) and the Fundamental Research Funds for the Central Universities (BHYC1702B, XK1802-6, and XK1803-05). Excellent support by Prof. Min Wei is gratefully acknowledged.

Author contributions
J.H. conceived the concept. X.X. and J.W. conducted the experiment and analysed the results. A.Z., S.D., B.L. and K.S. assisted in gas separation measurement. X.X. and J.H. wrote the paper and prepared the figures. All authors discussed the results. D.O'H co-supervised the research and revised the manuscript.

Competing interests
The authors declare no competing interests.

Additional information
Supplementary information The online version contains supplementary material available at https://doi.org/10.1038/s41467-021-23121-z.

Correspondence and requests for materials should be addressed to J.H. or D.O.

Peer review information *Nature Communications* thanks the anonymous reviewers for their contribution to the peer review of this work.